LARGE APERTURE, SPARSE MIMO PULSE-CODED SONARS: PRINCIPLES, FEASIBILITY AND IMAGING

O Malyuskin ECIT, Queen's University Belfast, UK
A McKernan
D Cooper
AJ Raj

1 INTRODUCTION

The study discusses the performance and imaging features of large-aperture, two- or three-dimensional sparse multiple input multiple output (MIMO) sonars operating in a narrowband pulse mode. In traditional single or multi-beam phased-array sonar systems, beam scanning in transmit mode is achieved through progressive time delay or phase difference between the adjacent transducers in the sonar array and coherent echo processing by the receivers[1]. MIMO sonars can generate space-time waveform diversity both in transmit and receive modes resulting in various imaging scenarios improving target resolution and acquisition speed or enabling cognitive target detection and tracking[2-4].

The operating features of MIMO communication systems, radars or sonars can be classified mainly using three categories: spatial multiplexing, spatiotemporal diversity and beamforming[5]. In this talk, we discuss how beamforming control can be achieved in both transmit and receive modes by using sonar transducers' selective switching, binary phase shift keying and pulse delay or pulse length coding. Time-domain beamforming enabled by these mechanisms creates spatiotemporal diversity of the radiated acoustic field in the sonar field of view (FoV) which creates the possibility of optimised acoustic illumination of the imaging scene. Time-domain processing of received echo signals allow to gather scene information in real time or almost real time with imaging resolution that depends on the sonar MIMO mode, sonar array geometry and the waveform parameters (frequency of operation, pulse length, etc.).

To improve image resolution acquired from the initial pulse snapshot, time-reversal[6] acoustic field localisation on the target or area of interest can be applied. Time-reversal digital signal processing implementation and time-processing constraints of the MIMO sonar system are briefly discussed in this paper with particular focus on the implementation using state-of-the-art embedded systems.

2 SONAR ARRAY BEAMFORMING

2.1 Sparse sonar radiated acoustic field and beamforming in transmit mode

Acoustic pressure $p(\vec{r},t)$ generated by a pulsed sonar array in unbounded space can be written, for a single ping, as a sum of the acoustic pressure waveforms (outgoing spherical waves) radiated by all *N* transducers of the array

$$p(\vec{r},t) = \sum_{n=1}^{N}\sum_{m=1}^{M} A_n \, sin[2\pi f(t-\tau_n - R_n/v) + s_{mn}] \, F_p(t,\tau_n,T_m,T_n) \frac{F_n(\theta,\phi)}{4\pi R_n} \quad (1)$$

In Eq.(1), $\vec{r}$ and $\vec{r}_n$ are the radius vectors of the observation position and the centre of the *n*-th transducer respectively, $A_n$is a peak acoustic pressure level at the output of the *n*-th transducer, *f* – centre frequency of the narrowband sinusoidal pulse, $R_n = |\vec{r} - \vec{r}_n|$, v is the speed of sound in the medium, $F_n(\theta,\phi)$ is an acoustic radiation pattern of the *n*-th transducer, Fig.1(a), (b). Parameters s_{mn} define the BPSK symbols and parameters τ_n, T_{mn}, T_n define the time delay of the *n*-th transducer

pulse, *m*-th BPSK symbol length and the overall pulse length, respectively, generated by the *n*-th transducer, Fig.1(c).

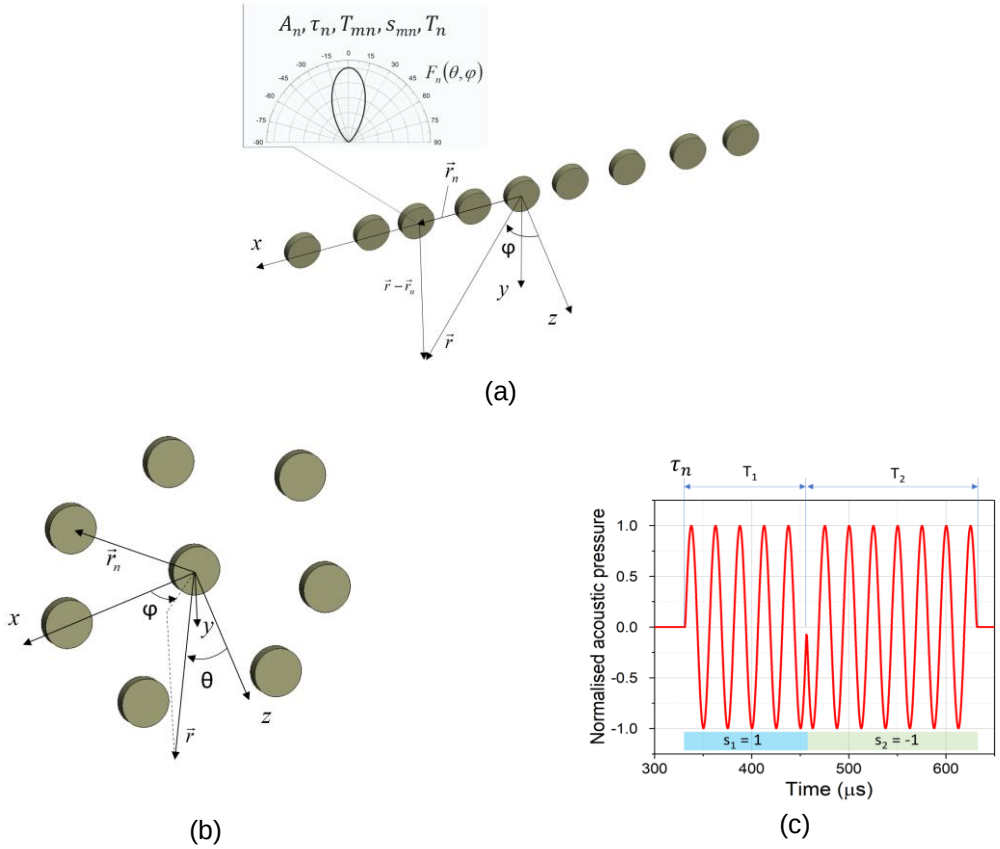

Figure 1. (a) 2D sonar array (b) 3D sonar array geometries and (c) sonar pulse parameters

Equation (1) is suitable for acoustic waveform description in an unbounded space, for example in a deep-water column. In the case of a complex scattering geometry, for example, a sonar, operating close to the water surface, several modelling approaches based on the asymptotic or ray approximations[5] can be efficiently employed using plane wave expansions of the spherical waves[7,8] in Eq. (1).

The typical geometry of a sparse, electrically large 2D (line sonar) and 3D (planar or volumetric) sonar is shown in Fig. 1(a), (b). It is important to note that due to sonar aperture sparseness and electrically large size, intense grating lobes appear in case of uniform spacings between the transducer elements which can be mitigated by using non-uniform (in particular, random) spacings or irregular lattice geometries[9].

2.2. Sonar beam characteristics in forward-looking mode: modelling examples

In this section, a practically important forward-looking sonar (FLS) scenario is numerically explored based on the model of Eq. (1) to demonstrate how MIMO sonar interoperability creates beamforming diversity which can be employed in FLS imaging by selective transmission by transducer elements.

Figure 2(a) shows the azimuthal cuts of the radiation patterns of normalised acoustic pressure in the water column generated by a sparse uniform line sonar array, operating at 50kHz and composed of 1, 3 and 11 transducers. The spacings between the antenna element are 10cm. Each transducer

radiates a conical beam with an angular half-bandwidth of 30º (at 3dB amplitude level). These modelling results show that the array radiation pattern gain is multiplicative of the number of transducers and the angular beamwidth is inversely proportional to the array aperture size. Even though in time-domain imaging the appearance of the grating lobes is not prohibitive for target detection, grating lobes mitigation can help deliver the acoustic energy in the FLS field of view (FoV) limited to narrower angles and improve signal-to-noise at the receiver. Grating lobes mitigation can be done by using non-uniform[9] sonar array apertures, Figure 2(b). The modelling results demonstrate the grating lobes suppression by at least 6dB, even for a small to moderate number of sonar transducers.

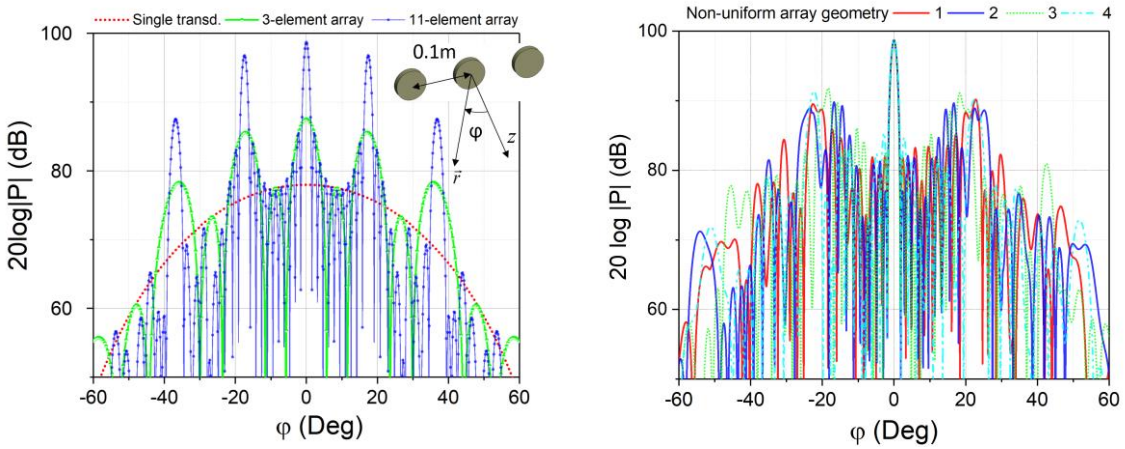

(a)

Figure 2. Normalised acoustic radiation patterns (azimuthal cuts) of a 2D line sonar array @50kHz in a deep-water column. (a) Effect of a number of elements on the radiation pattern of a uniform linear array. (b) Normalised radiation patterns of an 11-element non-uniform linear array with a total aperture length of 1m and transducer locations randomly arranged across the aperture with average spacings of 5cm. Lines 1-4 correspond to different random distributions of the transducers.

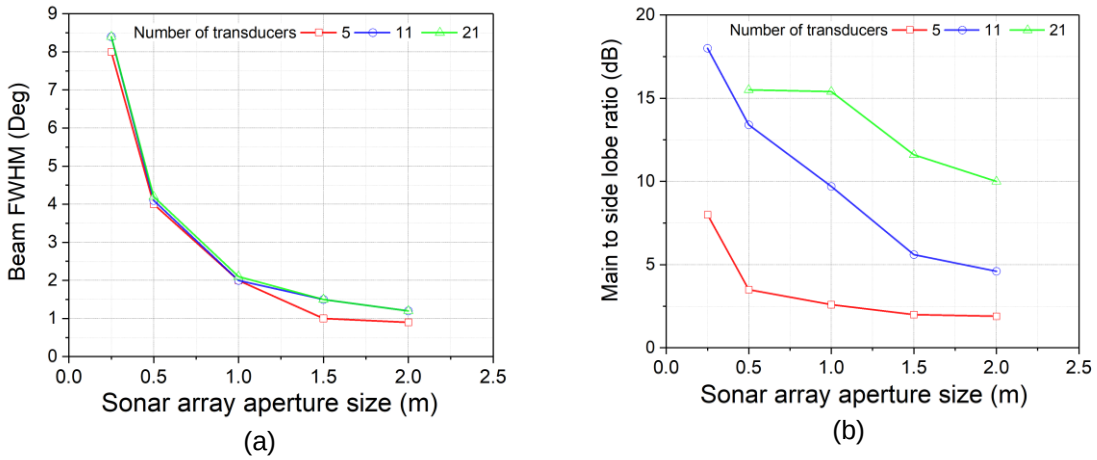

(a) (b)

Figure 3. (a) Full width at half-maximum (FWHM) of the sonar array main lobe beam (b) Main to side lobe ratio of the radiated acoustic beam for sonar arrays of various aperture sizes and number of transducers. The centre frequency is 50kHz.

The modelled spatial properties of the radiated acoustic patterns by a non-uniform linear sonar array with different numbers of transducers and array aperture sizes are shown in Figure 3. From Figure 3(a) it can be seen that the beam FWHM is inversely proportional to the array aperture size but does not significantly depend on the number of transducers in the array, when the number of transducers

exceeds certain value. However, the number of array transducers defines the main-to-side lobes ratio (or grating lobes amplitudes), which is demonstrated in Figure 3(b) showing a substantial decrease of the beam side lobes amplitude vs. the main lobe for a larger number of sonar transducers. Therefore using large sonar arrays results in a better combined signal-to-noise ratio at the receiver (for the same aperture size) however at higher complexity and cost of the sonar system.

An example of the simulated radiation patterns of circular and triangular cell planar sonar arrays is shown in Figure 4. It is interesting to note that the inner 7-elements sonar array, Figure 4(b),(d) has a notably better main-to-side lobe ratio as compared to the circular array, Figure 4 (a), (c) due to more efficient aperture utilisation.

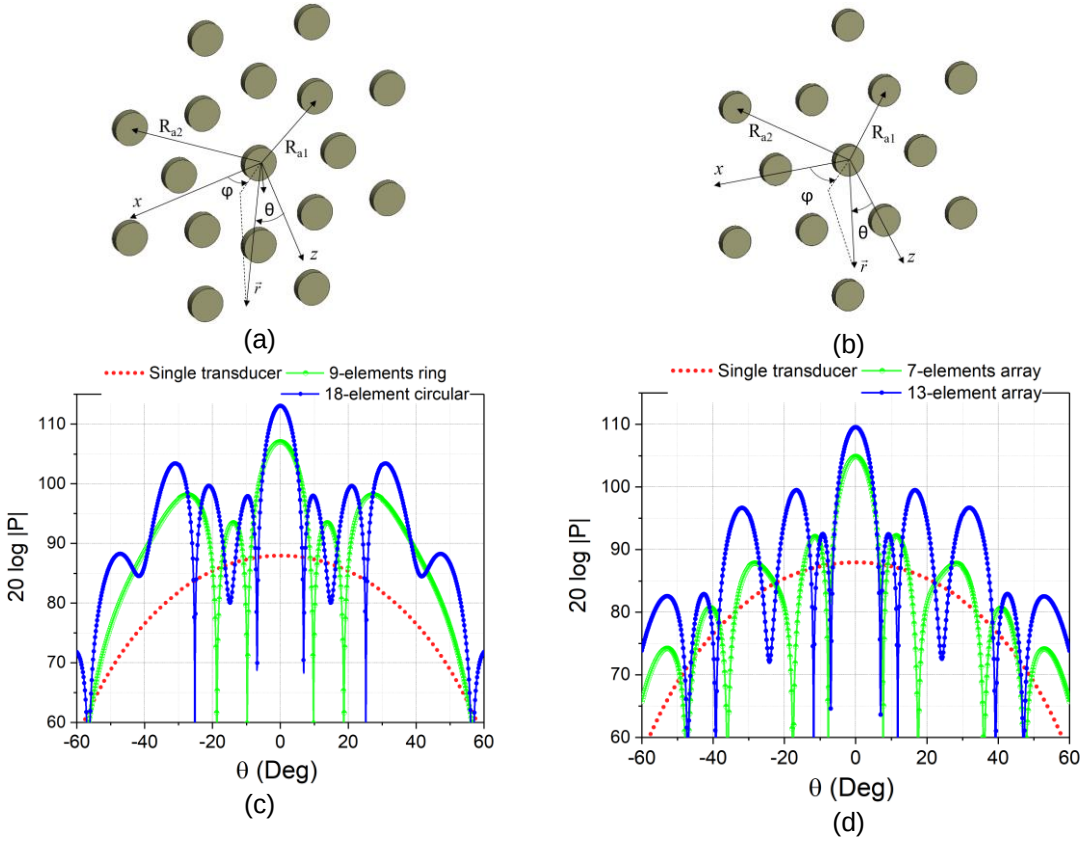

Figure 4. (a) the geometry and (c) acoustic radiation patterns (azimuthal cuts) of the circular array transducer array generated in a deep-water column for the parameters R_{a1}=75mm, R_{a2} = 125mm at 50kHz. (b), (d) radiation patterns of the triangular lattice array with 1, 7 and 13 elements.

2.3. Sonar beam shaping in forward-looking mode using BSPK and time-delay coding

BPSK coding across the sonar aperture results in interference of the radiated acoustic patterns leading to angular selectivity of the radiated acoustic beam, Figure 5(a). In the case of a uniform linear array, vector-space methods[10] based on the addition of waveforms in Eq. (1) can be applied to find analytical expressions for acoustical field distribution. For a randomly spaced transducer array, any suitable optimisation based on summing spherical waves in Eq.(1) can be applied to find the symbol distributions for the required angular directivity. The same BPSK aperture coding principle can be used to achieve sonar angular selectivity in the receive mode for the application of direction of arrival estimation of multiple reflected waves. From a physical point of view, BPSK pulse coding results in

the superposition of sum and difference beam patterns (for BPSK symbols ± 1 at the adjacent transducers) which can be used for both main and sidelobes nulls and maxima angular control of the radiated beam.

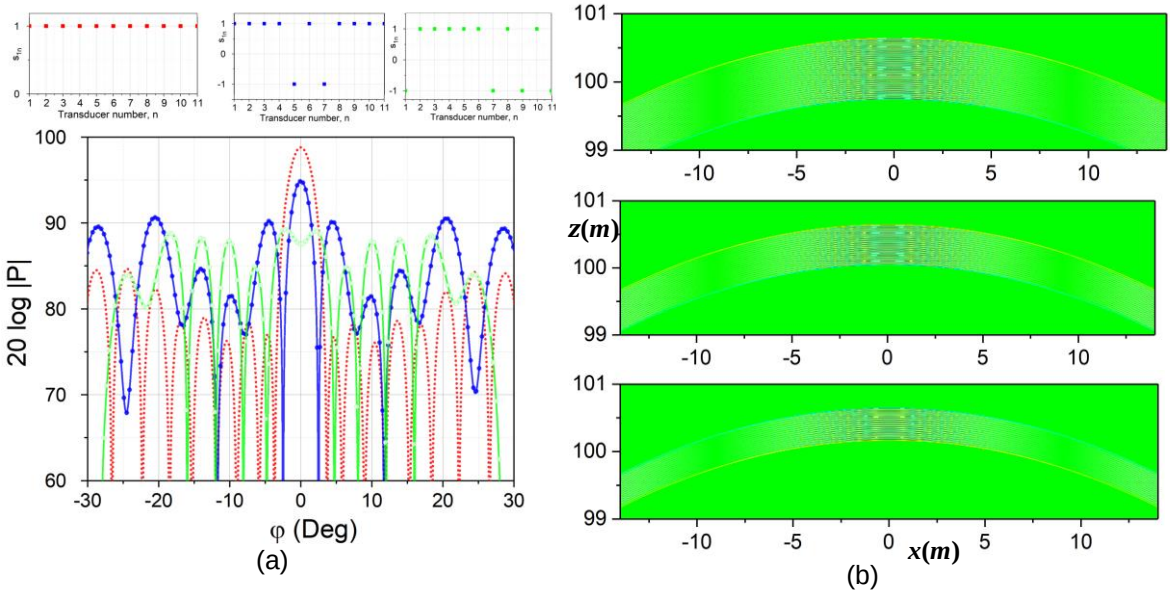

(a) (b)

Figure 5. (a) Radiated acoustic beams for an 11-element array with 0.5m aperture and random transducer locations at *f*=50kHz. The radiated beams are computed for 3 BPSK distributions shown in the insert above the graph. The waveform parameters are $T_1=35T_s$, $T_2=0$, $T_s=1/f$. (b) Spatiotemporal beam compression using a 4-element sonar transducer array with an aperture size of 0.3 m. Two outer transducers radiate synchronously while two inner transducers in the array radiate pulse-length coded waveforms with delays of $8.5T_s$ and $16.5T_s$ resulting in destructive interference and pulse length compression.

2.4. Time-reversal beamforming

Time-reversal imaging is based on wide-angle illumination of the imaging scene, recording the echo signals by an array of transducers, time-reversing these signals and re-applying to the sonar transducers in transmit mode. The coherent acoustic pulse radiated by the array then propagates back through the medium and refocuses approximately on the scattering targets leading to increased imaging resolution of the entire scan.

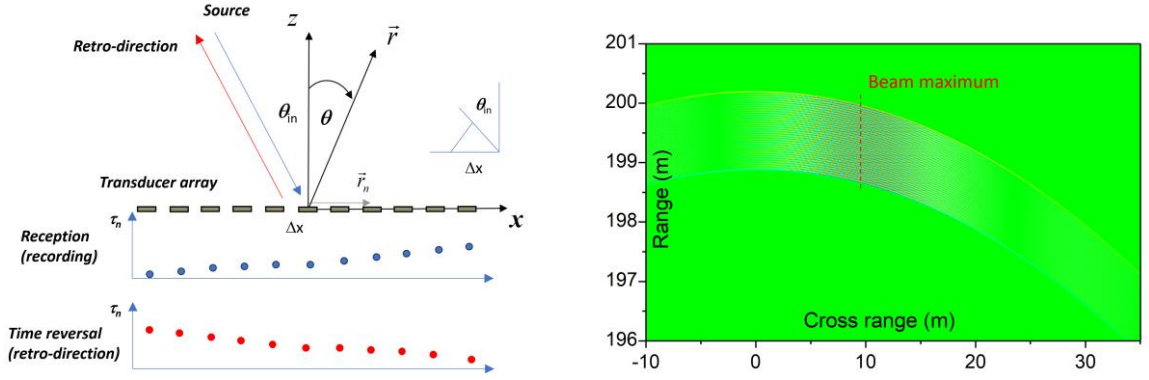

(a) (b)

Figure 6. (a) Schematic diagram of time-reversal time-delay beamforming. (b) A snapshot of a focussed pulsed beam by a 15-element non-uniform line transducer array with an aperture size of 1m and target location (10m,200m) at 50kHz.

From the geometry in Figure 6(a), the temporal resolution limit Δt of time-reversal processing is related to the angle of incidence θ_n (or, equivalently the angle of retro-direction) and transducer spacings Δx as $\Delta t = \Delta x \sin\theta_{in}/v$. Time resolution in a sonar system is defined by the performance limits of the digital signal processing core (with a typical characteristic time resolution of approximately 1μs) and analog front end, more specifically a transducer impulse response function. Another performance factor for time-reversal sonar is the angular resolution of the large aperture array, which is defined by the aperture size, e.g. Figure 3. A simulated example of time reversal sonar angular performance (15-element, non-uniform linear array of 1 m aperture at 50kHz) in Figure 7.

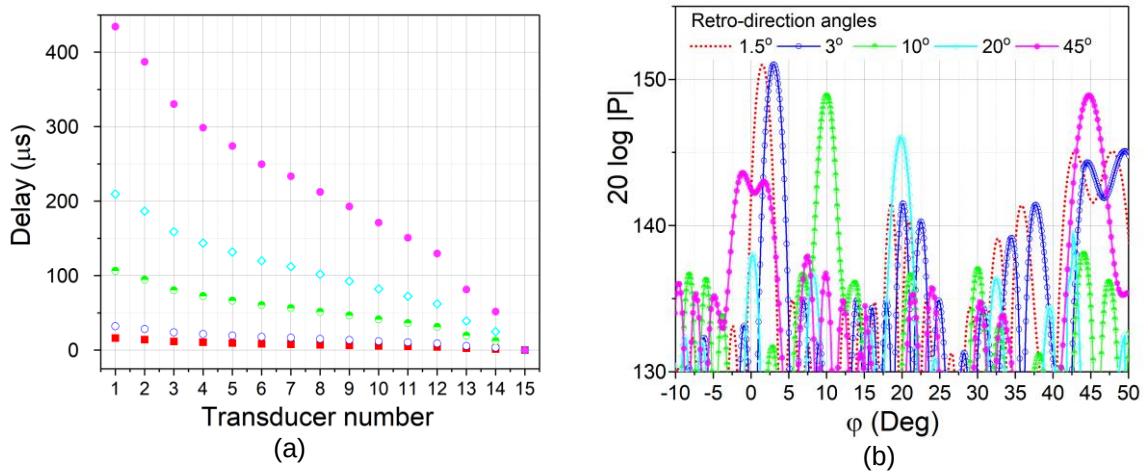

Figure 7. Simulated time-reversed beams for a non-uniform 15-element line transducer array of 1m aperture at 50kHz for various retro-direction angles. (a) time delays across the array aperture transducers. (b) azimuthal scans of the retrodirected beams.

3 MIMO SONAR IMAGING

In the FLS imaging mode, the targets in the sonar field of view (FoV) can be detected and characterised by processing the echo signals using cross-correlation functions C_{nm}, Eq.(2)

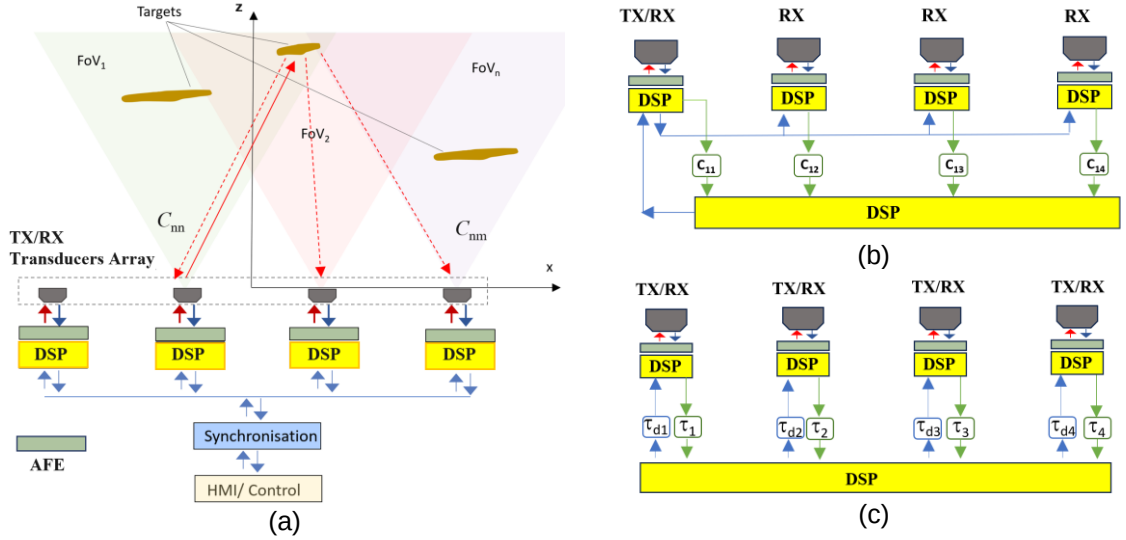

Figure 8. (a) Geometry of the FLS Imaging mode. (b) Multiple-input-single-output (MISO) imaging mode. (c) Time-reversal imaging mode. DSP- digital signal processing unit, AFE- analog front end.

$$C_{nm}(\tau) = \int_{t_0}^{t_0+T} s_{TX_n}(t-\tau)s_{RX_m}(t)dt \qquad (2)$$

Were s_{TX_n} is the signal generated by the n-th transducer signal in transmit mode and s_{RX_m} is a received signal (including ambient noise) by the m-th transducer in receive mode, Figure 8. The signal generation and echo processing (2) results in the cross-correlation matrix, {C_{nm}} capturing all possible signal transmission paths between the targets in the imaging area and elements in the pulsed sonar array. In the second step, the time-of-flight and target cross-range characteristics in the sonar field of view can be established by processing the cross-correlation peak and envelop information thus extracting the target positions and respective cross-range information.

In a MISO mode, Figure 8(b), the TX pulse onset time at the *n*-th firing transducer synchronises the reception (RX) across the array transducers. In the first-order approximation[13] in a sparse scattering scene, the k-th target can be detected and localised based on the set of equations involving time of flight between the n-th TX transducer, k-th target and the m-th RX transducer,

$$\left(x_t^{(k)} - x_n\right)^2 + z_t^{(k)2} = \left(t_{nm}^{(k)} v\right)^2 \; max(C_{mn}) > TH_{mn} \tag{3}$$

$$x_t^{(k)} = 0.5\left[(x_n + x_m) + \left(d_{nn}^{(k)2} - d_{nm}^{(k)2}\right)/(x_m - x_n)\right] \tag{4}$$

$$z_t^{(k)2} = d_{nn}^{(k)2} - \left(x_t^{(k)} - x_n\right)^2 \tag{5}$$

In Eq. (3)- (5), n is the index of a TX transducer and m is the number of the RX transducer, k-th target location in xz plane is given by coordinates $(x_t^{(k)}, z_t^{(k)})$, $t_{nm}^{(k)}$ is a time of flight between the n-th transducer, target and m-th transducer which is acquired from a maximum of the measured cross-correlation C_{mn}. $d_{nm}^{(k)} = t_{nm}^{(k)} v$ and TH_{mn} is an amplitude threshold for the C_{mn} peak value.

The imaging process involves dividing the imaging space into the ranges (or time of flight bins) in which the probability of detection (depending on the signal excess at the receiver, signal-to-noise, etc.) exceeds the required threshold and applying MISO, full-MIMO or time-reversal imaging modes.

4 INITIAL EXPERIMENTAL IMPLEMENTATION

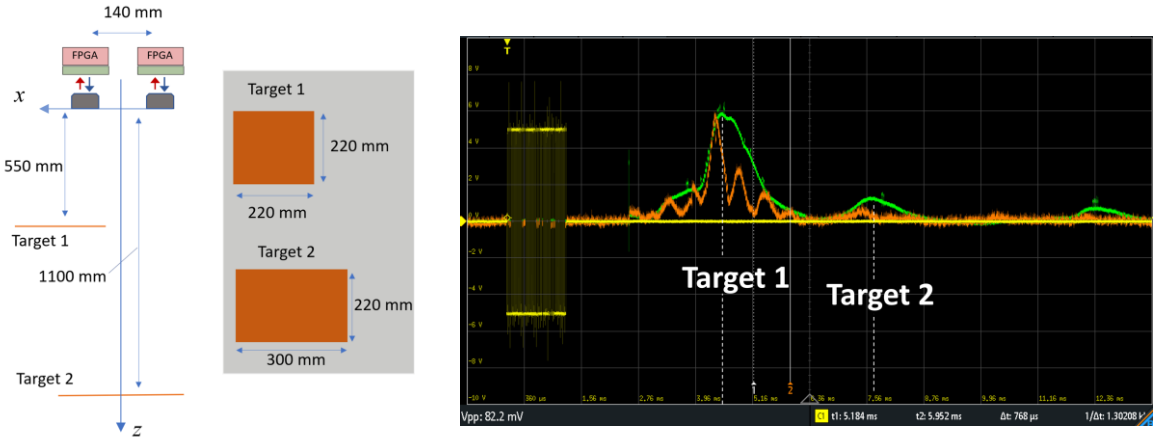

(a) (b)

Figure 9. (a) FLS imaging setup consisting of two large metallic targets in the air. (b) Measured cross-correlation of the received signals with a constant phase TX pulse (green line) and 5-Barker BPSK-coded TX pulse (orange line). Sonar frequency 40kHz. The targets images centres are localised at (120mm, 545mm) for Target 1 and (0mm, 1120mm) for Target 2.

To explore the feasibility of sparse large-aperture sonar imaging, a sonar prototype array has been fabricated using Xilinx Zynq 7010 field-programmable gate array (FPGA) and ARM Cortex M7/M9 microcontroller architectures[14] used as DSP programming core and custom-made analog front-end. MISO imaging results in a high signal-to-noise regime (high-visibility targets, low clutter environment) demonstrate good accuracy of single and multiple target localisation based on a MISO imaging model (3)-(5) even in the case of a two-element sonar array, Figure 9. Detailed imaging performance characteristics of the multi-element sparse sonar arrays in full MIMO and time-reversal modes will be reported in our future work.

5 CONCLUSIONS

Sparse large-aperture pulsed MIMO sonar arrays provide an alternative imaging method to conventional phased beam scanning sonars. In this study, the principle of operation of this class of sonars is discussed with a particular emphasis on beamforming and MIMO imaging algorithms which may offer several advantages such as faster imaging scene acquisition and acoustic illumination optimised for specific scattering scenes. Time-reversal beamforming is believed to be especially promising in the case of sparse array geometry due to relaxed requirements on the time synchronisation (as compared with dense phase arrays) and intrinsic self-focussing properties of the non-uniform linear or planar sonar arrays.

6 REFERENCES

1. A. D. Waite. Sonar for Practising Engineers. Wiley (2002).
2. I. Bekkerman and J. Tabrikian, ‘Target Detection and Localization Using MIMO Radars and Sonars’. IEEE Trans. Signal Proc. 54(10), 3873-3883 (2006).
3. X. Liu, et al., ‘High-resolution two-dimensional imaging using MIMO sonar with limited physical size’. Applied Acoustics, 182, 108280, (2021).
4. Y. Pailhas and Y. Petillot, ‘Neither PAS nor CAS: MIMO’, OCEANS 2016 (2016).
5. J. Bergin and J. R. Guerci. ‘Mimo Radar: Applications for the Next Generation’, IEEE Press (2018).
6. B. van Tiggelen and S. Skipetrov ed. Wave Scattering in Complex Media. From Theory to Applications. IOS Press (2002).
7. L.M.Brekhovskikh, Yu. P. Lysanov. Fundamentals of Ocean Acoustics. Springer, AIP Press (2003).
8. T. Hansen, A. Yaghjian. Plane-wave Theory of Time-domain Fields. IEEE Press (1999).
9. T. Torres, et.al.‘Low Discrepancy Sparse Phased Array Antennas’ Sensors (Basel). 21(23), 7816. (Dec 2021).
10. Y. Ding, V. Fusco, V. ‘A Review of Directional Modulation Technology’. Int. J. Microwave Wireless Tech. 8(7), 981-993 (2016).
11. C. Fei et al. ‘Difference beam aided target detection in monopulse radar’ Chinese Journal of Aeronautics, 28(5), 1485-1493 (2015).
12. W.S. Gan. Acoustical Imaging. Wiley (2012).
13. A. Tourin et. al. ‘Multiple scattering of sound’ Waves in Random Media10. R31–R60. (2000).
14. https://redpitaya.com/

ACKNOWLEDGEMENTS

This study was conducted as part of the Belfast Maritime Consortium UKRI Strength in Places project, ‘Decarbonisation of Maritime Transportation: A return to Commercial Sailing’ led by Artemis Technologies Ltd, Project no. 107138. The Authors thank Dr Benoit Lecallard, Artemis Technologies Ltd.'s technical team, and the SIP Programme Director Prof. Katrina Thompson for continuous support and insightful technical discussions.